Journal of the European Ceramic Society 43 (2023) 4588–4601

Contents lists available at ScienceDirect

Journal of the European Ceramic Society

journal homepage: www.elsevier.com/locate/jeurceramsoc

Elevated temperature tensile and bending strength of ultra-high temperature ceramic matrix composites obtained by different processes

Pietro Galizia [a,*], Diletta Sciti [a,*], Jon Binner [b], Vinothini Venkatachalam [b], Miguel.A. Lagos [c], Francesca Servadei [a], Antonio Vinci [a], Luca Zoli [a], Thomas Reimer [d]

[a] National Research Council of Italy, Institute of Science, Technology and Sustainability for Ceramics, CNR, ISSMC, Via Granarolo 64, 48018 Faenza, Italy
[b] School of Metallurgy and Materials, University of Birmingham, Birmingham B15 2TT, UK
[c] TECNALIA, Basque Research and Technology Alliance (BRTA), Mikeletegi Pasealekua 2, Donostia-San Sebastián 20009, Spain
[d] DLR German Aerospace Center, Institute of Structures and Design, Pfaffenwaldring 38-40, Stuttgart 70569, Germany

ARTICLE INFO

Keywords:
Ceramic Matrix Composite (CMC)
Ultra-High Temperature Ceramic Composite (UHTCMC)
Carbon fibre
High-temperature tensile strength
Residual Thermal Stress (RTS)

ABSTRACT

This paper presents a comparison of microstructures and mechanical properties of different ZrB_2-based CMCs, which were manufactured in the frame of the Horizon 2020 European C^{3}HARME research project through different processes: slurry infiltration and sintering (SIS), polymer infiltration and pyrolysis (PIP) and radio frequency chemical vapour infiltration (RF-CVI). Tensile testing with a novel optimized shape of the specimens was performed and compared with the results of flexural tests to assess the structural properties. For the first time, tensile tests up to 1600 °C were carried out on UHTCMCs. Despite the different microstructural features, all the ZrB_2-based CMCs demonstrated excellent structural properties even at elevated temperature. The characterization shows how the different amount of porosity and fibre properties, such as its stiffness, strength and elongation, affected the mechanical behaviour of the C^{3}HARME's composites. Finally, the role of the high level of residual thermal stresses is discussed.

1. Introduction

The novel class of ultra-high temperature (UHT) ceramic-matrix composites (CMCs), recognized as UHTCMCs, was extensively studied within the Horizon 2020 European research project entitled Next Generation Ceramic Composites for Harsh Combustion Environment and Space (C^{3}HARME) [1]. The sought-after applications of UHTCMCs developed in C^{3}HARME are thermal protection tiles and hot components for propulsion such as rocket nozzles and chamber inserts. Currently, these components are made of C/C or C/SiC composites which show low specific weight coupled with good structural properties, in terms of damage tolerance and strain to failure, but are not appropriate for components operating at ultra-high temperature above 1800 °C since they undergo oxidation and ablation [2–8]. To overcome these limits and improve the efficiency of the propulsion systems, and the durability of the thermal protection systems, an approach consists of adding ultra-high temperature ceramics (UHTCs) within the matrix [7–16, 17–19]. Among UHTCs, Zr-based borides or carbides are generally chosen owing to their high thermal conductivity (20–140 $Wm^{-1}K^{-1}$) and relatively lower density and cost compared to Hf or Ta based ones [20]. However, such composites, depending on the architecture of the reinforcing and fabrication process, have quite different features, in terms of UHTC and fibre content, matrix compactness, fibre/matrix interface, which are reflected in markedly diverse thermomechanical properties [21–26]. In a previous work [27], the C^{3}HARME Consortium dealt with temperature stability of several ZrB_2-based UHTCMCs by measuring their retained flexural strength after oxidation at 2005 °C. This previous study showed a promising oxidation resistance and an unexpected extremely high retained strength (even over 80%), although UHTCMCs are prone to thermal damage during heating [28–32]. However, no results of tensile strength at room and high temperature have been presented owing to the difficulty to obtain reliable values. In fact, although tensile testing is considered the most relevant standard to measure the strength of CMCs, no valid tensile tests with UHTCMCs were obtained following the current standards (ISO 14574:2013 for high temperature and 15733:2015 for room temperature).

In the present work, different types of UHTCMCs were produced through slurry infiltration and sintering (SIS), polymer infiltration and

* Corresponding authors.
E-mail addresses: pietro.galizia@issmc.cnr.it (P. Galizia), diletta.sciti@issmc.cnr.it (D. Sciti).

https://doi.org/10.1016/j.jeurceramsoc.2023.03.055
Received 6 February 2023; Accepted 26 March 2023
Available online 29 March 2023

pyrolysis (PIP) or radio frequency chemical vapour infiltration (RF-CVI) process. The presented UHTCMCs differed from each other not only for the production process but also for the type of matrix and fibres and their architecture. In particular, the volume percentage of UHTC in the matrix among the composites ranged from 8 to 49 vol%, uncoated pitch-derived carbon fibre or PyC-coated PAN-derived carbon fibre were used and the architectures consisted of in-plane randomly oriented short fibres, unidirectional continuous fibre fabrics stacked in 0/90° configuration or 2.5D needle punched arrangement. As for the mechanical characterization, the elastic moduli were measured at RT, while the tensile strength was measured at RT and 1600 °C by using a new specimen geometry that was designed in the frame of the C^{3}HARME project [1]. The tensile testing campaign suggested that the designed shape is promising to reduce the number of invalid tests and can be integrated in the norm ISO 14574:2013 and 15733:2015. Finally, flexural strength at RT and elevated temperature (up to 1800 °C) was measured. The flexural tests together with the tensile tests allowed a more complete cross mechanical characterization among the investigated UHTCMCs and a deeper understanding of their different mechanical behaviour.

2. Experimental

2.1. Materials manufacturing

The compositions, fabrication technologies and other information of fabricated materials are reported in Table 1. All compositions contained ZrB_2 (Grade B, H.C. Starck, Germany) and SiC (Grade UF-25, H.C. Starck, Germany), while different commercial fibres were used.

a) *Sintered short fibre composites* (labelled as SFC) were manufactured by mixing ZrB_2 plus SiC powder with pitch C_f milled down to a length of 150 μm (Nippon Graphite Fibre Corporation, HC-600) through dry mixing. The mixture was consolidated by Nanoker Research S.L. (Spain) in their hybrid SPS furnace H-HP D 400 (FCT System GmbH, Germany).
b) *Sintered continuous fibre composites* (labelled as CFC) were produced as follows: the powder mixture consisting of ZrB_2 plus SiC was prepared by wet ball-milling and drying by a rotary evaporator. With this mixture, an aqueous slurry was prepared using poly-acrylates as dispersant. The composites were fabricated by infiltrating unidirectional fabrics (Nippon Graphite Fibre Corporation, UF-XN80-300) stacked in a 0/90° arrangement. The green assembly, a disc of 400 mm diameter and 10 mm thickness, was sintered by Nanoker Research S.L. (Spain) in their hybrid SPS furnace H-HP D 400 (FCT System GmbH, Germany).
c) *PIP composites* (labelled as PIP) were fabricated via the filament winding and PIP process developed by Airbus (former EADS) and currently used to manufacture the SICARBON™ material [33]. Pyrolytic carbon coated continuous carbon fibres (T800HB-6000–40B, Toray Industries Inc., Japan) were infiltrated with a slurry of a pre-ceramic SiC polymer, SiC, ZrB_2 and Ta powders through filament winding technique. The obtained unidirectional fabrics were stacked in a 0/90° configuration, cured in an autoclave and pyrolyzed at 1600 °C in nitrogen atmosphere. Three re-infiltration steps with a pre-ceramic SiC polymer and following pyrolysis were carried out with the aim to reduce the porosity resulting from the organic-to-inorganic conversion process.
d) *CVI composites* (labelled as CVI) were prepared using 2.5D continuous C_f preforms (obtained from PANOX, 23 vol% C_f, Surface-Transforms plc., Cheshire, UK) with fabric layers stacked in an arrangement of random/0°/random/90°/random orientation fibres, where 0° and 90° are unidirectional layers, in plane and out of plane respectively and the random layers were formed as a result of Surface Transform's needling process. An ethanol based slurry containing ZrB_2, nano particles of SiC and Y_2O_3 and polyethylene imine (PEI) dispersant was introduced into the 2.5 D preform by a manual injection process [34]. After injection, the preforms were cleaned and dried in an air oven and further densified with pyrolytic carbon using a radio frequency (RF) heated chemical vapour infiltration process (RF-CVI).>

2.2. Microstructure characterization

Phases volumetric amounts and fibre contents were measured by image analysis on the polished surfaces of the samples where possible. Theoretical density values were calculated from these amounts, while geometric density was measured on the machined specimen bars. From the experimental-to-theoretical density ratio, relative density and porosity were calculated. The microstructures were analysed by FESEM (FE-SEM, Carl Zeiss Sigma NTS Gmbh Oberkochen, Germany).

2.3. Brief introduction of the new geometry designed for the tensile specimens

The existing standards for tensile testing of CMC materials (ISO 14574:2013 for high temperature and 15733:2015 for room temperature) give certain sample shapes which should be used. In view of some constraints of the material development not all the shapes are equally suitable. For instance, in the C^{3}HARME project, as in practically every other material development program, plates are fabricated having a

Table 1
Process details: green preparation method; consolidation techniques. Fibre details taken from the suppliers: type and architecture; density (ρ_{fibre}); elastic modulus (E_{fibre}); strength (σ_{fibre}), elongation (ε_{fibre}) and orientation efficiency factor (η_0) obtained through Krenkel approach [36]: $\eta_0 = \Sigma\, a_n \cos^4 \theta_n$, where a_n is the fraction of fibres oriented along the angle θ_n with respect to the direction of the applied load. Composite characteristics: compositions expressed as volumetric amount of ceramic phases, fibre and porosity (P), and measured geometrical density (ρ).

	Process		Fibre details						Composite characteristics				
	Green Preparation	Consolidation technique	Type and architecture	ρ_{fibre} g/cm^3	E_{fibre} GPa	σ_{fibre} MPa	ε_{fibre} %	η_0	Matrix vol%	Coating vol%	Fibre vol%	P vol %	ρ g/cm^3
SFC	Fibre mixing	SPS	Pitch, Milled fibres	2.22	860	3430	0.4	0.38	49ZrB_2 10SiC	-	40	1	4.1
CFC	Slurry impregnation	Hybrid SPS	Pitch, 0/90°	2.17	780	3430	0.5	0.48	36ZrB_2 4SiC	-	54	6	3.5
PIP	Filament winding	PIP	PyC-coated PAN, 0/90°	1.81	294	5880	1.9	0.5	6(ZrB_2, TaC) 20SiC	16	33	25	1.9
CVI	Manual injection	RF-CVI	PANOX, 2.5D	1.7[a]	215[b]	1750[b]	-	0.4	30ZrB_2 37PyC	-	23	10	2.9

[a] Value measured through mercury intrusion porosimetry.
[b] Value took from Ref.[80].

limited thickness, making the use of rotationally symmetric samples quite difficult and those geometries are not an option. For this reason, the shape most commonly used is the so-called dog-bone sample, with a wider section at the ends, where the sample is clamped, and a narrow straight section in the centre. The transition from the wide ends to the narrow section is achieved with radii. From earlier investigations in the frame of the C^{3}HARME project, it was known that with this sample shape, there were problems due to stress concentrations at the transition from the radius to the narrow section, causing failure there at higher stress than the nominal stress in the straight test section. This was mainly due to the very low failure strain of the ceramic materials in combination with the lack of plasticity. However, with straight samples there was the problem of the influence of the clamping, leading to stress concentrations at the clamps. In fact, it was found that also the straight samples led to unsatisfying results with mostly invalid results due to fracture at the clamping.

In view of these problems, a new shape of the tensile specimen (reported in Fig. 1) was designed through finite element analysis based on the properties of the new UHTCMCs developed. The idea was to find a reasonable compromise between the dog-bone shape and the straight non-tapered sample, aiming for the largest possible shoulder radius within a given total length of the sample which was prescribed by the project manufacturing constraints. The numerical simulations showed that the stress peak in a dog-bone sample is always located at the transition from the radius into the straight calibrated section and that the amount of the stress overshoot depends on the radius size. For a dog-bone sample with a clamping width of 15 mm and a calibrated width of 10 mm and a 30 mm shoulder radius, the stress overshoot at the transition was roughly 25% compared to the stress in the center of the calibrated section. By reducing the length of the calibrated section to only 10 mm and increasing the radius to 240 mm, the stress overshoot could be reduced to just 4% compared to the nominal stress in the calibrated test section which was seen as acceptable. In the center of the sample, a short section of 10 mm uniform width was retained for the purpose of installing strain measurement sensors in RT testing.

2.4. Mechanical characterization

Young's modulus, tensile strength at room temperature and 1600 °C, bending strength at room temperature, 1600 °C, 1800 °C were measured, as explained below.

The in-plane and off-axis Young's modulus of the composite (E and $E_{\perp}$, respectively) and the in-plane shear modulus (G) were measured through the sonic resonance frequency analysis on three 60 mm × 10 mm × 2.5 mm (length, width, and thickness) bars in agreement with the ASTM C1198 – 09 standard.

Tensile strength (σ_t) tests were conducted at the German Aerospace Center (DLR, Stuttgart). The tests followed the EN 658–1:1999 norm for tests at room temperature and the ISO 14574:2013 norm for tests at high temperature with the modified geometry reported in Fig. 1. All the samples with continuous fibre in these tests had a fibre alignment of 0/90°, so fibres were running in the longitudinal direction and transverse. On the contrary, CVI samples available for tensile strength tests had a fibre alignment of + /- 45°. The notable dimensions of the specimens, with a length of 170 mm, required the capability to scale-up the various processes. For SFC and CFC, 400 mm discs were successfully sintered by SPS [35]. The room temperature tensile tests were carried out in a standard mechanical test machine of the type Zwick-Roell 1475. The data recorded were the force and the displacement. In addition, an optical measurement system based on Digital Image Correlation (DIC) principles was employed to measure the strain field of the samples without contacting them (Fig. 2a). The samples were coated with a suitable black and white colored tracking pattern for this reason. Two cameras were used in front of the sample and two dedicated light sources were used to have a more controlled lighting situation. In Fig. 2b one example of the strain field during the test is shown. The evaluation of the strain was done as taking the average over a rectangle in the centre section of the sample as shown in Fig. 2b. In the data evaluation, the stress is based on the recorded force applied on the nominal cross section.

For tensile strength tests at 1600 °C, a special high-temperature testing facility, called INDUTHERM and available at DLR, was used. The heating of the sample was done indirectly via radiation from a heated graphite cylinder surrounding the sample. A high-frequency AC

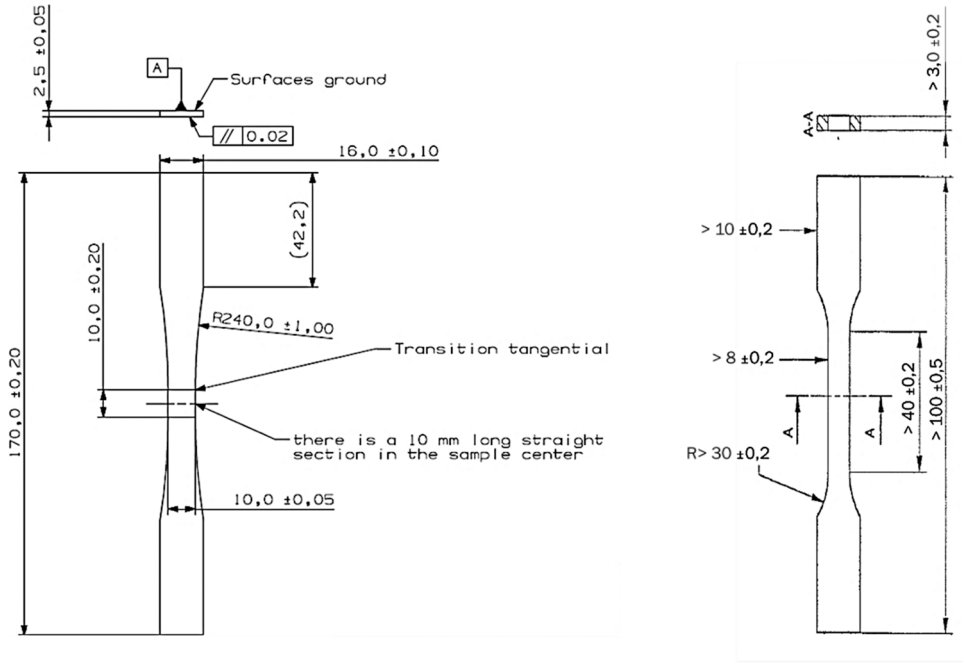

Fig. 1. On the left, drawing of the newly developed tensile sample shape. In the sample centre, there is a 10 mm long straight section. On the right, dog-bone specimen geometry suggested in ISO 15733:2015.

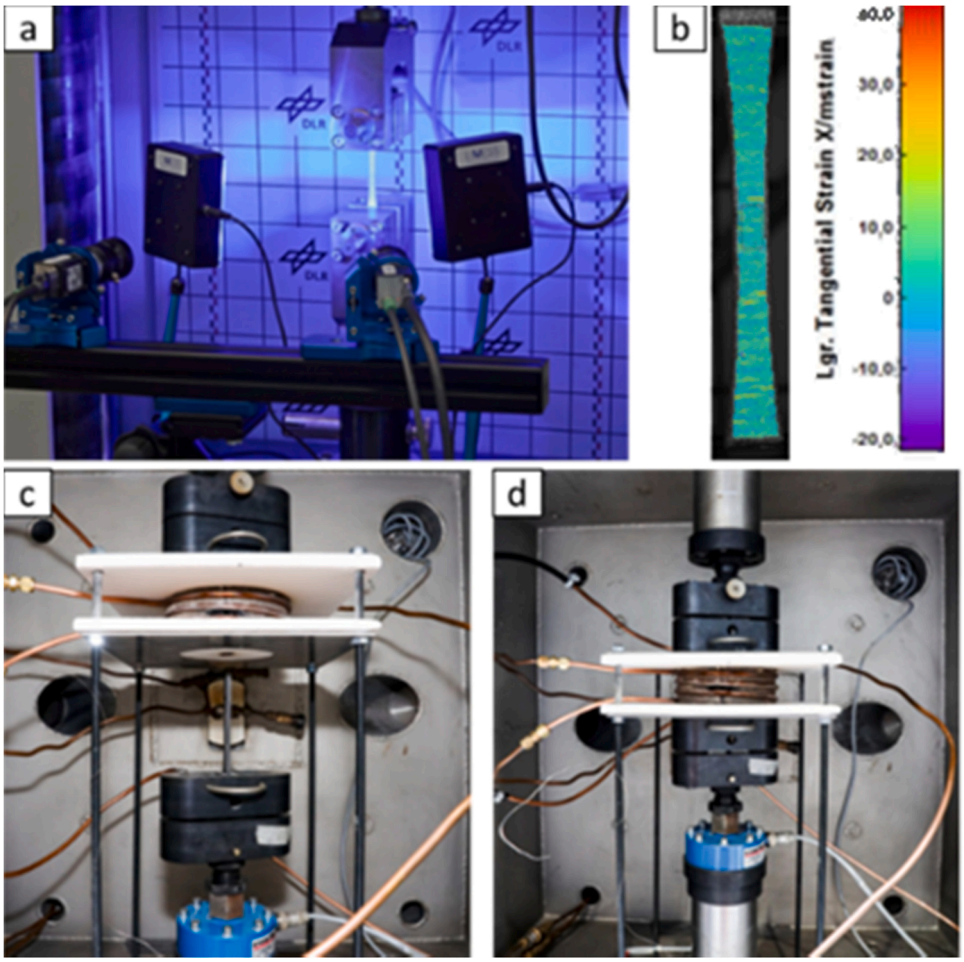

Fig. 2. (a) Room temperature tensile testing setup making use of DIC strain measurement. (b) Typical optical strain measurement via DIC during test; value is given as millistrain. (c and d) High temperature tensile test setup with sample retracted from the heating device (c) and in position for testing (d).

current with a power of 50 kW was used to heat the graphite cylinder via induction by a surrounding coil. The sample and the induction heating were located inside a water-cooled vacuum chamber. Tests can be done under nitrogen or argon at variable pressure or in vacuum. The temperature inside the graphite cylinder was controlled via a pyrometer, using a hole in the graphite cylinder, the pyrometer itself was placed outside the vacuum chamber, looking through a window in the chamber front door. The setup of the test is presented in Fig. 2c and d. In Fig. 2c, a sample was clamped with the cylinder retracted, so that the sample was out of the heating device. In Fig. 2d, the sample was moved up into the heating device and clamped on both ends. The clamps were water cooled.

Flexural strength (σ_f) at RT and high temperature was tested by 3-point bending test on 60 mm × 10 mm × 2.5 mm (length, width, and thickness) bars, with a span of 50 mm and a crosshead speed of 8 mm/min. All the samples with continuous fibre (CFC, PIP and CVI) in these tests had a fibre alignment of 0/90°, so the tensile and compression stresses were applied in the longitudinal direction and transverse direction of the fibres. The stress (σ) and the strain (ε) were calculated according to the following equations:

$$\sigma = \frac{3Fs}{2wt^2} \quad (1)$$

$$\varepsilon = \frac{6Dt}{s^2} \quad (2)$$

Where F is the force, s is outer support span, w and t are the specimen width and thickness, respectively, and D is the deflection. Bending tests at RT were carried out in a Zwick-Roell Z050 screw-driven load frame. High temperature bending tests at 1600 °C or 1800 °C in argon flux were carried out in the INDUTHERM machine available at DLR (Fig. 3).

3. Results and discussion

3.1. Microstructure

Table 1 summarizes processes, compositions and main microstructural features of the four UHTCMCs. Further details are described in the following paragraph.

3.1.1. Sintered short fibre-reinforced composites (sample ID: SFC)

were characterized by a fully dense microstructure with 40 vol% of milled fibres randomly distributed (see Table 1 and Fig. 4a). The SiC was homogeneously dispersed in the ZrB_2 matrix and the fibres (Fig. 4b), 150 μm long, were well anchored to the matrix. The smooth fracture surface and limited fibre pull-out (about 5 μm) confirmed the high densification of the matrix and the strong fibre/matrix adhesion, Fig. 4c. A camera picture of as sintered SFC tile with diameter of 400 mm is shown in Fig. 4d.

3.1.2. Sintered 0/90° continuous fibre-reinforced composites (sample ID: CFC)

displayed a fibre volumetric content higher than SFC (54 vs 40%), whilst a comparable near-full matrix densification was obtained (Fig. 5). The higher porosity (6 vs 1%) was ascribed to the presence of inter-fibre

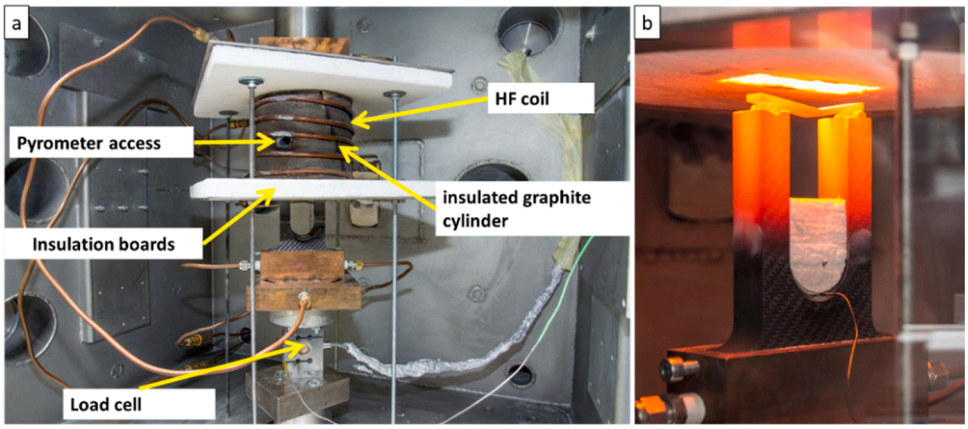

Fig. 3. (a) Test setup for high-temperature 3-point bending tests in the INDUTHERM facility. (b) Load introduction on the lower side with sample on the roller bars.

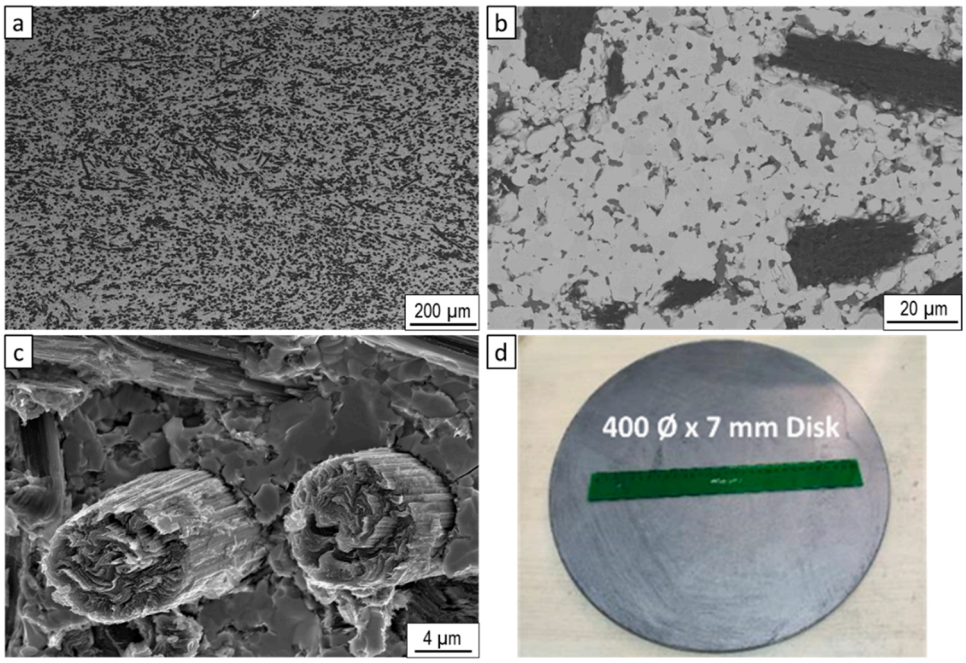

Fig. 4. SEM of (a,b) polished and (c) fracture surface of SFC. (d) Camera pictures of as sintered SFC. The micrographs show the texture, fibre distribution in the matrix, matrix features, matrix/fibre interface features and fibre pull-out.

pores within the fibre clusters whose fibres were not completely dispersed during slurry impregnation, leaving porosities and weak fibre/fibre interfaces upon densification [37,38]. Fibres (black) and SiC (dark grey) were homogeneously distributed in the dense ZrB_2 matrix (light grey), see Fig. 5a-d, and the jagged fibre/matrix interface suggested a strong adhesion as attested also by the limited fibre pull-out of about 10 µm (Fig. 5e). Unlike SFC, the high matrix densification and the strong matrix/fibre interfaces led also to matrix micro-cracking perpendicular to the fibre axis due to coefficient of thermal expansion (CTE) mismatch between matrix and fibre and the anisotropy of the unidirectional layers. The fabrics infiltration, their hand layup, and the sample machining resulted in an in-plane fibre misalignment that ranged from 2° to 10° with an average value of 8°. This fibre misalignment coupled with the 0/90° architecture led to a Krenkel factor (η_0) of 0.48 (η_0 is 1 for unidirectional fibres perfectly aligned in the loading direction and 0.5 for ideal 0/90° composites [36]).

3.1.3. 0/90° continuous fibre-reinforced composites fabricated via PIP (sample ID: PIP)

showed an uniform fibre distribution in the matrix and good alignment (Fig. 6a). In a similar material produced by Airbus with the same process and filament winding parameters, the fibre kept an average misalignment within 1° [33]. Considering the fibre diameter of 5.3 µm, and the PyC-coating thickness of 0.6 µm [33], there is an effective volumetric fibre content of 33 vol%. As observed through EDS analysis (Fig. 6b), the brightest particles are TaC (fine particles smaller than 1 µm), while the light grey particles are ZrB_2 (coarse particles up to 6 µm). Among the composites studied in the present work, PIP material showed the lowest density of 1.9 g/cm^3, which mainly reflected the high porosity of 25 vol% (all phases but carbon fibres have a density higher than 1.9 g/cm^3: PyC ~2.1–2.2 g/cm^3 [39], polymer derived SiC ~2.8–3.2 g/cm^3 [39], ZrB_2 ~6.1 [40] and TaC ~14.5 g/cm^3 [41], respectively). The large porosity is something which was expected and desired to fabricate a weak matrix composite characterized by higher toughness [42,43]. In fact, 7–9 PIP cycles are necessary to yield the final porosity below 10 vol% [44–49]. The high amount of porosity resulted

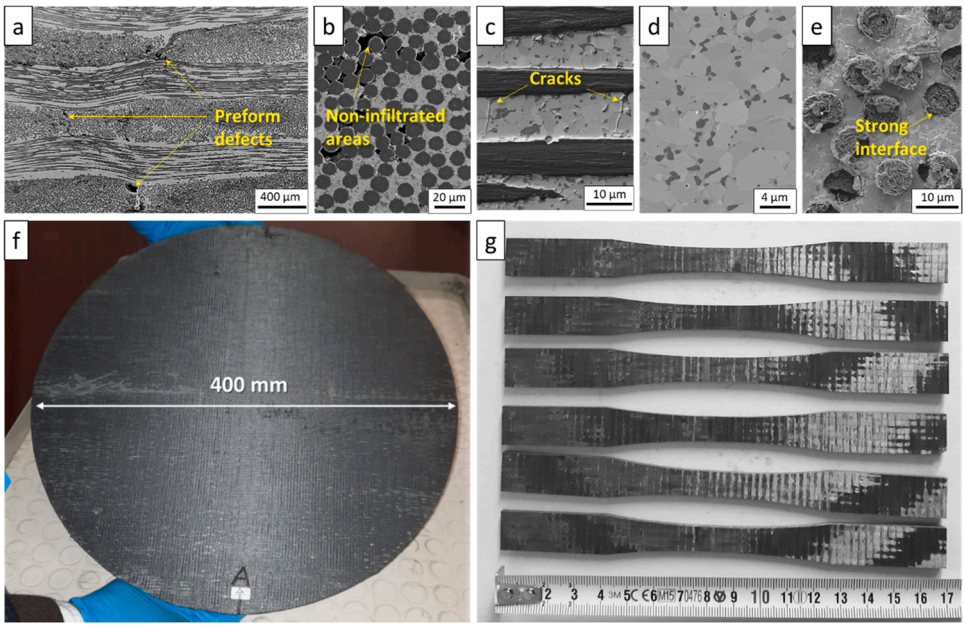

Fig. 5. SEM of (a-d) polished and (e) fracture surface of CFC. Camera pictures of (f) as sintered SFC and (g) extracted dog bone bars for tensile strength tests. The micrographs show the texture, fibre distribution in the matrix, matrix features and fibre pull-out.

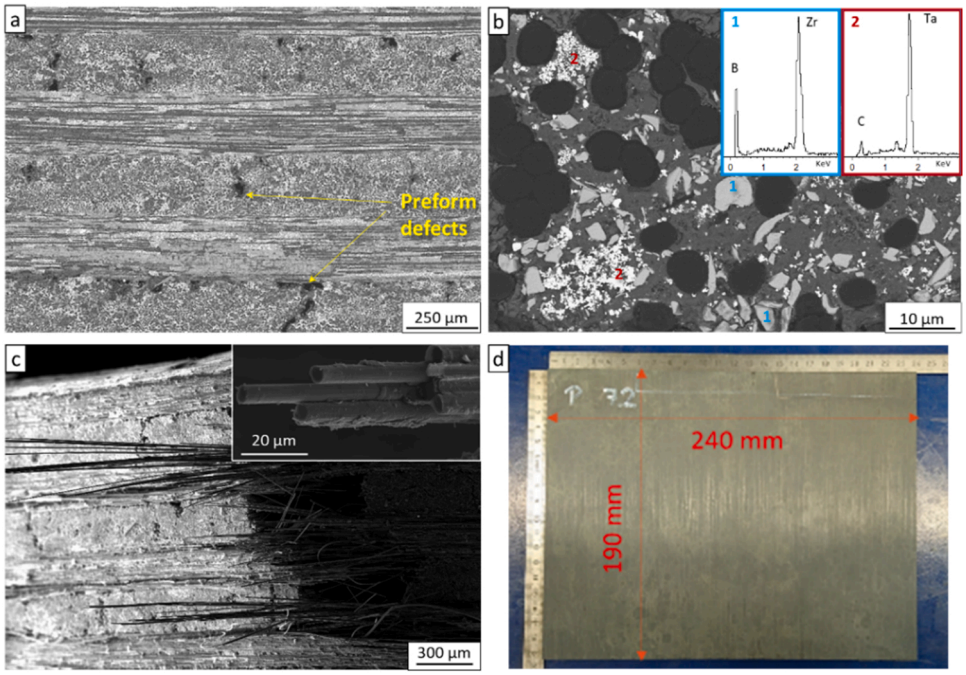

Fig. 6. SEM of (a,b) polished and (c) fracture of PIP. (d) Camera pictures of a consolidated PIP plate. The micrographs show the texture, fibre distribution in the matrix, matrix features and fibre pull-out.

in an extensive fibre pull-out (see Fig. 6c) occurring at the matrix/-coating interface (Fig. 6c inset). A 190 × 240 mm^2 plate was fabricated to machine bars for the mechanical characterization (Fig. 6d).

3.1.4. 2.5D fibre-reinforced C/C-ZrB_2 composites fabricated via CVI (sample ID: CVI)

were constituted by 2.5D fibre-reinforced C/C composites doped with 15% ZrB_2. The complex 2.5D preform architecture is outlined in Fig. 7a. The PyC/C_f matrix is represented by the dark regions, while the coarse white particles are ZrB_2 (Fig. 7b). Large pores appeared as black isolated spots. The fracture surface (Fig. 7c) shows an extensive fibre pull-out allowed by the detachment of the fibre from the powderized ZrB_2-PyC matrix.

3.2. Mechanical properties

3.2.1. Sintered short fibre-reinforced composites (SFC)

The highest Young's modulus (180 GPa, see Table 2) was obtained for SFC material that is characterized by low porosity (1 vol%) and crack-free matrix. The highly densified matrix and the fibre volumetric content lower than 50 vol% amount contributed to obtain the high off-axis modulus of 80 GPa. This value is higher than that of sintered 0/

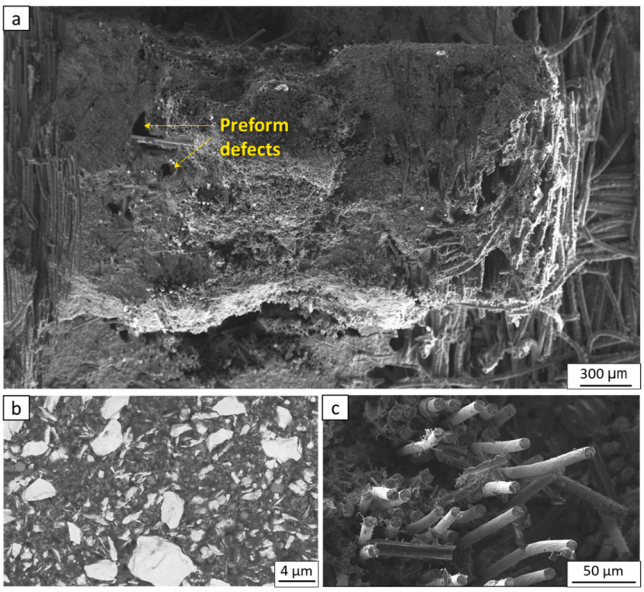

Fig. 7. SEM of fracture surfaces of CVI. The micrographs show the texture, fibre distribution in the matrix, matrix features and fibre pull-out.

0° continuous fibre-reinforced composites (about 70 GPa [29]), which are characterized by a fibre volumetric content higher than 50 vol% and microcracked matrix.

3.2.2. Tensile strength and bending strength

In Fig. 8a, the tensile curves of the SFC material showed a predominantly brittle failure at low strain values (about 0.5‰). The failure displacement values are the lowest of all materials tested. The absence of strong evidence of toughening mechanisms at RT is generally ascribed to the reduced fibre length (150 µm) and the strong adhesion of the fibres to the full dense matrix. At 1600 °C the tensile curves were almost linear up to fracture which occurred at higher stress: 100 MPa instead of 80 MPa obtained at room temperature. Similar results were obtained through bending tests (Fig. 8b). In terms of the maximum stress values, there is no significant difference between the tests at RT, 1600 °C and 1800 °C. If anything, it could be said that all the tests done at elevated temperature gave higher values than the room-temperature one, which suggests that the strength is probably increasing from room to high-temperature testing and the stress-displacement curves changed from being linear to non-linear. Concerning the fracture displacement, i.e. the strain at fracture, there seems to be a trend towards higher strain with increasing temperature. The calculated strain changed from 0.0008 at RT to 0.0014 at 1600 °C and to 0.0034 at 1800 °C. Similar short fibre-reinforced ZrB_2 [50] showed more evident toughening phenomena and a pretty much higher flexural strength (458 vs 126 MPa) owing to the longer fibre (1–2 mm vs 150 µm) and half of volumetric fibre content (20 vs 40 vol%).

3.2.3. Sintered 0/90° continuous fibre-reinforced composites (CFC)

The Young's modulus and G modulus of CFC were 137 and 25 GPa, respectively, Table 2. The high volumetric amount of high modulus fibres (780 GPa according to the supplier) was not reflected in the measured in-plane Young's modulus of CFC material because (i) the 0/90° architecture should almost halve the value and (ii), according to

Table 2
Mechanical properties.

	Sonic resonance: elastic moduli			Tensile testing: strength (σ_t) and strain (ε_t)			Flexural testing: strength (σ_f) and strain (ε_f)					
	E GPa	$E_\perp$	G	σ_t MPa	$\sigma_{t1600°C}$	ε_t ‰	σ_f MPa	$\sigma_{f1600°C}$	$\sigma_{f1800°C}$	ε_f ‰	$\varepsilon_{f1600°C}$	$\varepsilon_{f1800°C}$
SFC	181 ± 2	81 ± 4	17 ± 1	80 ± 18	100 ± 8	0.5 ± 0.1	127 ± 6	152 ± 14	159 ± 6	0.8	1.4 ± 0.2	3.4 ± 0.3
CFC	137 ± 6	-	25 ± 1	120 ± 7	200 ± 24	2.5 ± 0.5	178 ± 22	-	316 ± 20	4.1 ± 0.4	-	4.6 ± 1.5
PIP	63 ± 1	16[a]	4[a]	219 ± 11	339 ± 18	3.6 ± 0.5	242 ± 24	-	-	5.9 ± 0.8	-	-
CVI	28 ± 3[b]	-	-	79 ± 8[b]; 28 ± 8[c]	57 ± 7[c]	-	167 ± 86	170 ± 129	147 ± 39	11.4 ± 5.4	18.6 ± 8.6	53.3 ± 44.6
LSI[d]	50–70	20	6.6	80–190	-	1.5–3.5	224	-	-	-	-	-

⊥Properties measured on bars vertically machined (pile-up direction in case of continuous fibres).
[a] From Ref. [33].
[b] From Ref. [71].
[c] Specimens tested with a fibre alignment of + /- 45°.
[d] Reference C/C-SiC composite developed by DLR through liquid silicon infiltration process (LSI) from literature [51,60].

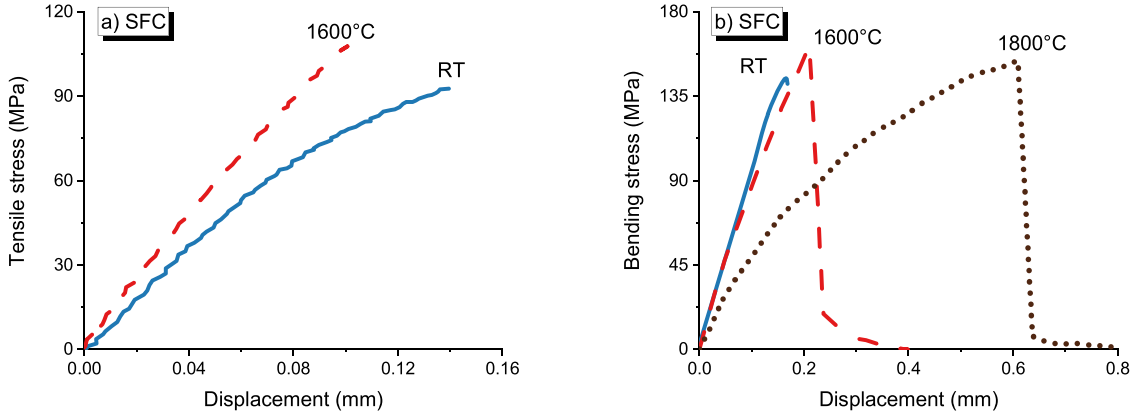

Fig. 8. Typical stress-displacement curves of sintered short fibre-reinforced composites (SFC label) at room temperature (solid blue curves) and high temperature (dashed red curves and dotted black curve for tests at 1600 °C and 1800 °C, respectively) of (a) tensile tests and (b) bending tests.

classical laminate theory and the 25 GPa of measured shear modulus, the estimated 8° misalignment of the fibres should decrease the value by about another 40%. As for the matrix of CFC material, it is expected a Young's modulus of the matrix lower than 200 GPa owing to the presence of microcracks [28].

3.2.4. Tensile strength and bending strength

Tensile strength was 120 MPa at RT and increased to 200 MPa at 1600 °C. Bending strength was higher, 178 MPa at RT and 316 MPa at 1800 °C, see Table 2. As for stress-displacement behaviour of CFC material, the stand-out characteristic is the evident three-stage deformation [37] before fracture in both tensile and bending tests at room temperature (Fig. 9a,b). This breaking in steps behaviour, evidenced in Fig. 9b, is typical of damage tolerant CMCs and could be justified with the ACK model [55]. However, the stiffness recovery in the last stage in some case, unlike the expected theoretical behaviour, is comparable to the pristine value. This peculiar behaviour visible in Fig. 9a,b was observed also in bending tests of specimens with small geometry carried out at the earliest stage of development of these composites [27,56] as well as in large specimens (200 mm in length) currently under tensile testing. This evidence is in contrast with the commonly observed stiffness reduction due to the matrix cracking [57,58]. Whilst the reason of maintenance, or even increasing, of the stiffness after matrix cracking is not yet fully understood, the lower stiffness of the second stage is due to matrix cracking and consequent release of the residual compressive strain of the fibres [37]. In fact, the releasing of the compressive strain leads to an increment of the displacement although the increment of the applied load is equal to zero. The long extension of this second stage needs further study to understand if this stage is controlled by just strain release or other phenomena, such as sliding at the matrix/fibre interface or sliding of the graphene sheets inside the onion type pitch fibre. The main role played by the residual thermal stress (RTS) is also supported by the remarkably different stress-strain behaviour recorded at high temperature, where the second stage is no longer evident, and the trend of the curve appears bilinear due to the release of residual thermal strain. The increase of stiffness was observed with the reference LSI material [59,60] and also C/SiC composites produced via CVI [61]. The increase of strength [61–64] was attributed to the combination of the increase of strength of carbon fibres with temperature [65] and the possible matrix-cracking that allowed the release of RTSs [28] and a better alignment of fibre along the stress field [29]. This is in agreement with the behaviour of reference C/C-SiC composite and other CMCs [64,66,67] where the release of thermally-induced tensile stresses in the matrix was considered responsible for strength increase at elevated temperature. Like SFC material, the bending stress-displacement curves at 1800 °C showed a softening tendency. However, CFC withstood higher strains to failure: up to five times (Table 2).

3.2.5. 0/90° continuous fibre-reinforced composites fabricated via PIP (PIP)

The off-axis modulus of 20 GPa should be attributed to the high porosity, the incompletely converted polymer derived SiC, and the high volumetric content of pyrolytic carbon [33,44,45]. In agreement with these microstructural features and the lower modulus of the fibre (294 GPa according to the supplier), the in-plane Young's modulus of the PIP material resulted in about 60 GPa, which is comparable with the value of the reference LSI composite as well as the transverse Young's modulus and the in plane shear modulus.

3.2.6. Tensile strength and bending strength

The tensile tests at RT of the PIP material (Fig. 10 a) showed the highest value of strength, 219 MPa (see Table 2), and a quite linear behaviour up to fracture. The bending strength, recorded just at room temperature, was 242 MPa. The linear behaviour recorded during tensile suggests a perfect bond that allows a constant load transfer between matrix and fibres till failure, similar to the linear elastic behaviour of carbon/carbon composites [52]. Although it is commonly reported that for these composites matrix and fibre fracture occurs at the same strain [52], the authors of the present work think that the matrix fails at a much lower strain, between 3 and 24 times lower than that of the composite (0.0036). This range was calculated by dividing the measured strain to failure of 0.0036 with the calculated strain to failure of the matrix as the ratio of matrix strength (3–25 MPa [33,68]) to matrix modulus (20 GPa [33]). For the same reason, in a previous work [33], the maximum proportional limit stress/strain (PLS_{max}) was defined as the stress at 5% deviation from the linear segment extrapolated from the range where the slope was maximum. In this way, the loss of linearity, which occurs in a wide range of small strains due to the failure of the matrix dominated 90° layer, was not taken into account and the onset of composite failure has been made to coincide with the onset of the fibre failure (about 25% lower than the maximum strength). The remarkable higher tensile strength, 219 MPa at RT and 339 MPa at 1600 °C, of PIP material compared to that of CFC material (80% higher at RT and 70% at 1600 °C) should be partially referred to the higher strength of the T800 fibre with respect to XN80 one (5880 vs 3430 MPa, according to the suppliers). In fact, the product of the theoretical strength of T800 per its volumetric fraction in the PIP material is 11% higher than the product of the theoretical strength of XN80 per its volumetric fraction in the CFC material. The remaining gap between the measured tensile strengths could be ascribed to the better fibre alignment allowed by the automated filament winding process, the better stress transfer from matrix to fibre due to the presence of pyrolytic carbon coating, the lower stress concentration due to the weak matrix, and/or by the retained strength of the PAN-derived fibres since they were not subjected to sintering treatments.

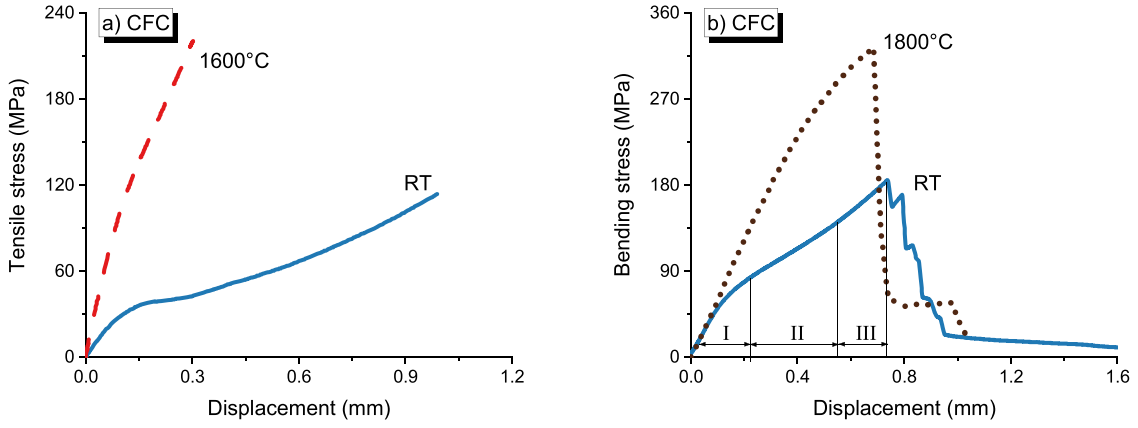

Fig. 9. Typical stress-displacement curves of sintered 0/90° continuous fibre-reinforced composites (CFC label) at room temperature (solid blue curves) and high temperature (dashed red curve and dotted black curve for tests at 1600 °C and 1800 °C, respectively) of (a) tensile tests and (b) bending tests.

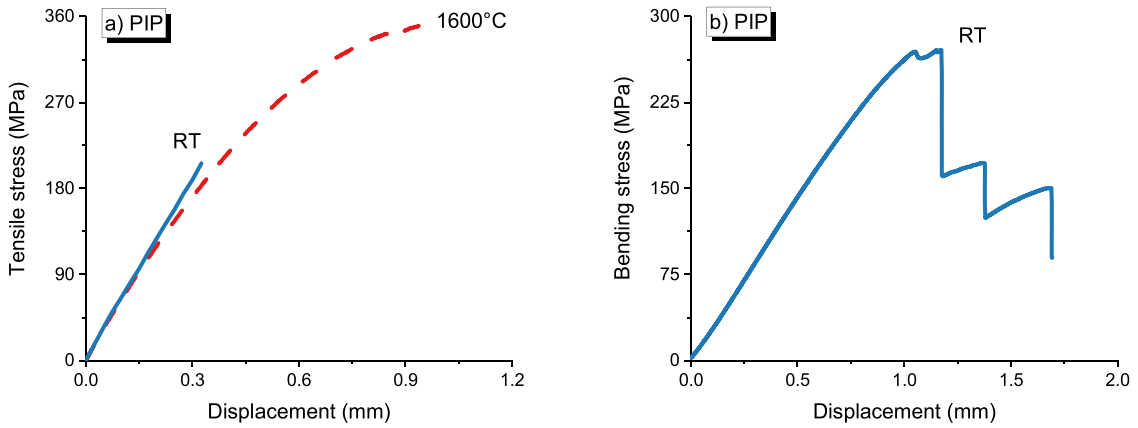

Fig. 10. Typical stress-displacement curves of 0/90° continuous fibre-reinforced composites fabricated via PIP (PIP label) at room temperature (solid blue curve) and 1600 °C (dashed red curve) of (a) tensile tests and (b) bending tests.

At 1600 °C, the tensile strength increased from 200 to 230 MPa to 320–350 MPa due to the release of thermal residual stresses [69]. The activation of softening mechanisms at 1600 °C could be due to the high volumetric SiC-to-UHTC ratio and the lower temperature of the pyrolysis process with respect to the sintering process (1600 vs 1900 °C). In fact, SFC and CFC materials showed signs of softening only at 1800 °C thanks to the higher amount of highly dense UHTC phase (49% and 36%, respectively, see Table 1) and absence of residual soft phases. In fact, UHTCMCs fabricated by PIP showed a strong increase of their thermal stability after further consolidation via HP at 1900 °C [70].

3.2.7. 2.5D fibre-reinforced C/C-ZrB_2 composites fabricated via CVI (CVI)

The lowest Young's modulus, of about 30 GPa, was obtained for CVI material that is characterized by lowest amount of carbon fibre with complex architecture and largest amount of PyC (see Table 1).

3.2.8. Tensile strength and bending strength

CVI samples displayed a damage tolerant behaviour (Fig. 11 a), thanks to the weak matrix/fibre interface. However, the resulting tensile strength was quite low, due to the + /- 45° fibre orientation. The tensile strength of about 80 MPa along 0/90° direction, measured with dog-bone specimens (300 mm × 24 mm × 9 mm, length by width by thickness) [71], falls within the range of reference LSI composite. In addition, the samples showed a pronounced step-wise fracture along the 45° angle, also as a result of the different fibre alignment. Looking at the tensile tests at 1600 °C, also CVI material showed a significant influence of the temperature. The two samples tested at 1600 °C went up to roughly twice the stress than the samples tested at room temperature. In case of bending tests (Fig. 11 b), the large scatter around the mean values is indicative of the different fibre architectures of the specimen after machining. In fact, since the bars have smaller dimensions with respect to the representative volumetric element of fabric preform, the tests gave high or low values depending on whether the outer surface under tensile stress had a prevalence of longitudinal, transverse or random fibre orientation. This architecture variability was also reflected in the tests at high temperature, where the first thing which stands out here is that two samples showed a very distinct plasticity at 1800 °C, leading to a much higher failure strain than it was the case for the other CVI samples, and in fact also for all the other SFC and CFC samples. This reduction of stiffness was observed from the beginning of the test and may be attributed to a specific prevalence of fibre architecture and not only to the temperature, because there was one sample, which was not showing this behaviour at 1800 °C.

3.3. Comparison amongst the composites

Tensile tests with the novel specimen's geometry yielded good results in terms of the collected data (Fig.s 8a, 9a, 10a, 11a) and in terms of failure mode and location. As expected, there is plenty of difference in the mechanical responses among the UHTCMCs, here presented, due to the different composition, type and volume content of fibre, fibre/matrix interface and fibre arrangement. However, the obtained strength values are within the range of values reported in the literature [22] for other CMCs with a non-UHTC matrix. In general, the developed

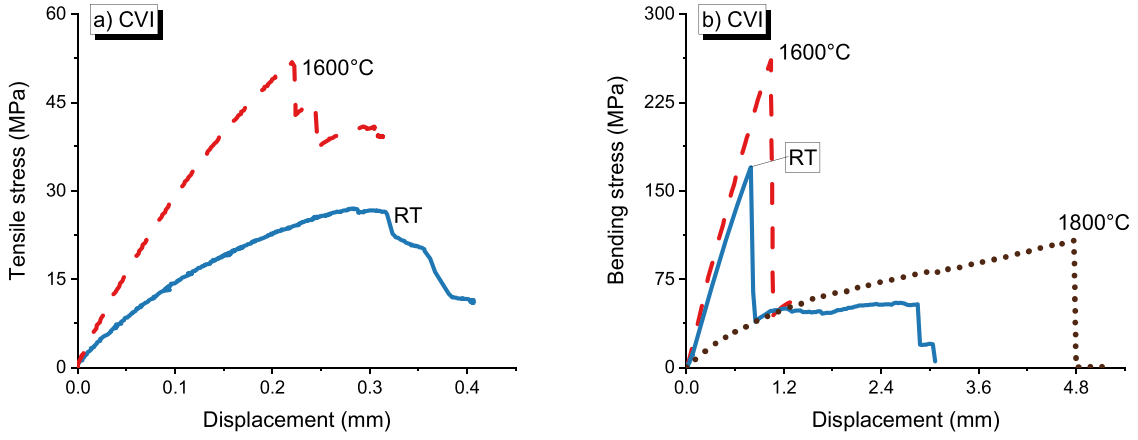

Fig. 11. Stress-displacement curves of 2.5D fibre-reinforced C/C-ZrB_2 composites fabricated via CVI (CVI label) at room temperature (solid blue curve) and high temperature (dashed red curve and dotted black curve for tests at 1600 °C and 1800 °C, respectively) of (a) tensile tests and (b) bending tests.

UHTCMCs mostly displayed comparable or better strength and stiffness than C/C-SiC composite produced via liquid silicon infiltration process (LSI) [60]. Amongst them, only short fibre reinforced composites display a brittle behaviour, due the peculiar microstructural features, previously described.

In general, it can be noted that there was a large variation in the resulting strength as well as in the displacements (strain) that were reached. Also, the stiffness was very different and mainly linear e.g. for the SFC and PIP materials, whereas in the case of other materials it is more or less decreasing with strain. It is worth noting that at RT, in the case of CFC materials, the stiffness decrease is only apparent in the second stage and the pristine stiffness is recovered in the third stage. This is the only one atypical mechanical response that was never previously reported in literature for other CMCs and was attributed to the residual thermal stresses (RTSs) [37]. As for other CMCs, the flexural strength of all UHTCMCs was found to be higher than tensile strength [36,51,52]. This is usually due to (i) the lower effective volume under tensile stress in a bending test [36], (ii) different stresses redistribution under the flexure stress gradient [53], (iii) transverse and shear stress concentrations close to the grips; and/or (iv) shift of the neutral plane owing to the changing of tensile-to-compressive modulus caused by matrix cracking [51,54]. For all the investigated UHTCMCs there seems to be an influence of the temperature on the strength with higher strength at higher temperature. Regarding the tensile tests, the highest strength and strain to failure were obtained for the PIP material with 340 MPa and 0.0036, respectively. This outstanding mechanical response was mainly attributed to the higher strength and elongation of the PAN-derived fibre, in addition to an optimized matrix fibre interface, and a greater degree of freedom of the fibres allowed by the presence of the PyC coating and weak matrix. In second place, there is clearly the sintered CFC material with also high strength (up to 200 MPa) and a failure to strain under tensile loading at RT of 0.0025. This material also showed a strong increase of strength and stiffness with increasing the temperature, mainly in tensile testing. The stiffness of the SFC material is also very high, but the ultimate strength is significantly lower. However, unlike PIP material, UHTCMCs showed no softening mechanisms at 1600 °C. For the CVI material, the picture is not very clear due to the different fibre texture of the tensile specimens and the dimension of the bending specimens smaller than the representative volumetric element of fabric preform. However, the presented results of CVI material complement the previously published characterisation [71] showing the tensile behaviour along the + /- 45° direction of the fabric preform and the changing of the flexural response with the increasing of temperature. In order to unravel the correlations between microstructural characteristics (Table 1) and mechanical properties (Table 2) of the C^{3}HARME composites a correlation matrix was determined calculating Pearson correlation coefficients (r), Fig. 12. The colour scale legend spans from red for positive correlations (r > 0) to blue for negative correlation coefficients (anti-correlations). It is worth noting that the stronger the tendency is, the larger is the absolute value of the correlation coefficient. Due to the lack of a guideline for interpretation of the correlation coefficients (r) [72], and the complex interactions among the different parameters [36], we arbitrarily chose r = |0.5| as lower boundary to define if two variables are correlated. The main results are as follows.

The Young's modulus of all the composite (E) was well correlated to the Young's modulus of the fibre ($r = 0.99$), in agreement with the Voigt's equation (rule of mixtures)

$$E = E_{fibre} V_{fibre} \eta_0 + E_{matrix}\left(1 - V_{fibre}\right). \quad (3)$$

The same strong positive correlation ($r = 0.99$) was found for the Young's vs the fibre density, which is obvious since modulus and density are strongly correlated to each other [73]. Also, the inverse correlation between E and the porosity ($r \cong -0.7$) is supported by the Voigt's equation (Eq. 3), if the detrimental effect of porosity (P) on the Young's modulus of the matrix is taken into account [28,74].

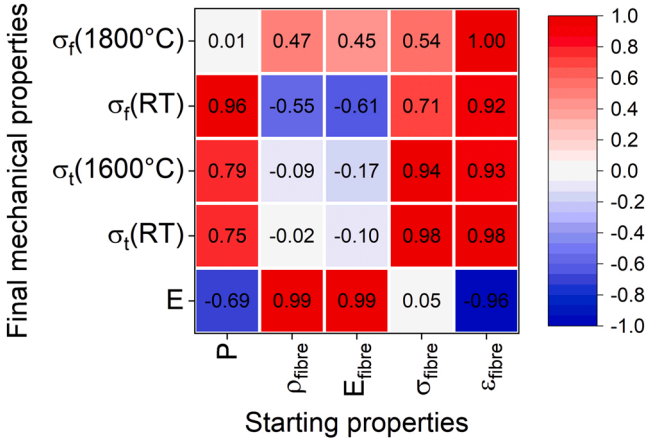

Fig. 12. Pearson correlations between microstructural features, reported in Table 1 (P: porosity; ρ_{fibre}: fibre density; E_{fibre}: fibre modulus; σ_{fibre}: fibre strength; ε_{fibre}: fibre elongation), and the mechanical properties of the C^{3}HARME composites, reported in Table 2 (E: Young's modulus; σ_t(RT): tensile strength at RT; σ_t(1600 °C): tensile strength at 1600 °C; σ_f(RT): flexural strength at RT; σ_f(1800 °C): flexural strength at 1800 °C). |0.5| was arbitrarily chosen as lower boundary to define if two variables are correlated.

Finally, even the correlation between porosity and strength of the C^{3}HARME composites agree with the composite literature [75]. The lack of correlation ($r \cong 0$) in case of flexural strength at 1800 °C can be explained by the significantly higher strength of CFC material due to its higher thermomechanical stability (i.e. less prone to softening mechanisms) and release of RTSs. The matrix seems to suggest some correlation ($r \cong |0.6|$) between the stiffness of the fibres and the flexural strength of the composites. The inverse correlation at RT suggests that the fibre's stiffness decreased the apparent interlaminar shear strength of the composites leading to a lower flexural strength. In fact, this decrease was not observed with the tensile tests ($r < |0.2|$) where the interlaminar shear stresses are negligible. This result agrees with a previous work, Ref. [33], where we observed a decrease of apparent interlaminar shear strength with the increase of the composite's stiffness as consequence of the different span-to-thickness ratio. At 1800 °C this effect is hidden and exceeded by the strength gain due to the higher thermomechanical stability (i.e. the composites with higher stiffness were less prone to softening mechanisms). Finally, as expected the strength of the C^{3}HARME composites shows a good correlation with the strength and the elongation of the fibres.

3.3.1. *Peculiarities of UHTCMC with respect to the SoA: the high level of Residual Thermal Stresses*

As previously discussed, the obtained mechanical properties are correlated to the different microstructures as predicted by the conventional models of CMCs. However, CFC material at RT showed an atypical non-linear behaviour that was not shown by other C^{3}HARME materials and CMCs more in general. This peculiar behaviour is thought to be due to the high level of RTS. In agreement with Ref. [37], the effect of RTS on mechanical behaviour can be observed through the first derivative of the load-displacement curves of the mechanical tests. The stiffness vs displacement curves of all the C^{3}HARME composites, obtained from the tensile and bending tests at room and high temperature, are plotted up to the point of failure, Fig. 13. SFC, PIP and CVI can be described via a monotonically non-increasing function, in agreement with the decrease of elastic modulus with the accumulation of damage described by continuum damage mechanics (CDM) models [76,77]. In contrast, the curves of CFC composite at RT are not monotonic. The stiffness degradation for hundreds of microstrains and its following recovery is a novelty in the field of CMCs and was attributed to the release of the fibre compressive strain, as consequence of the matrix cracking (decreasing

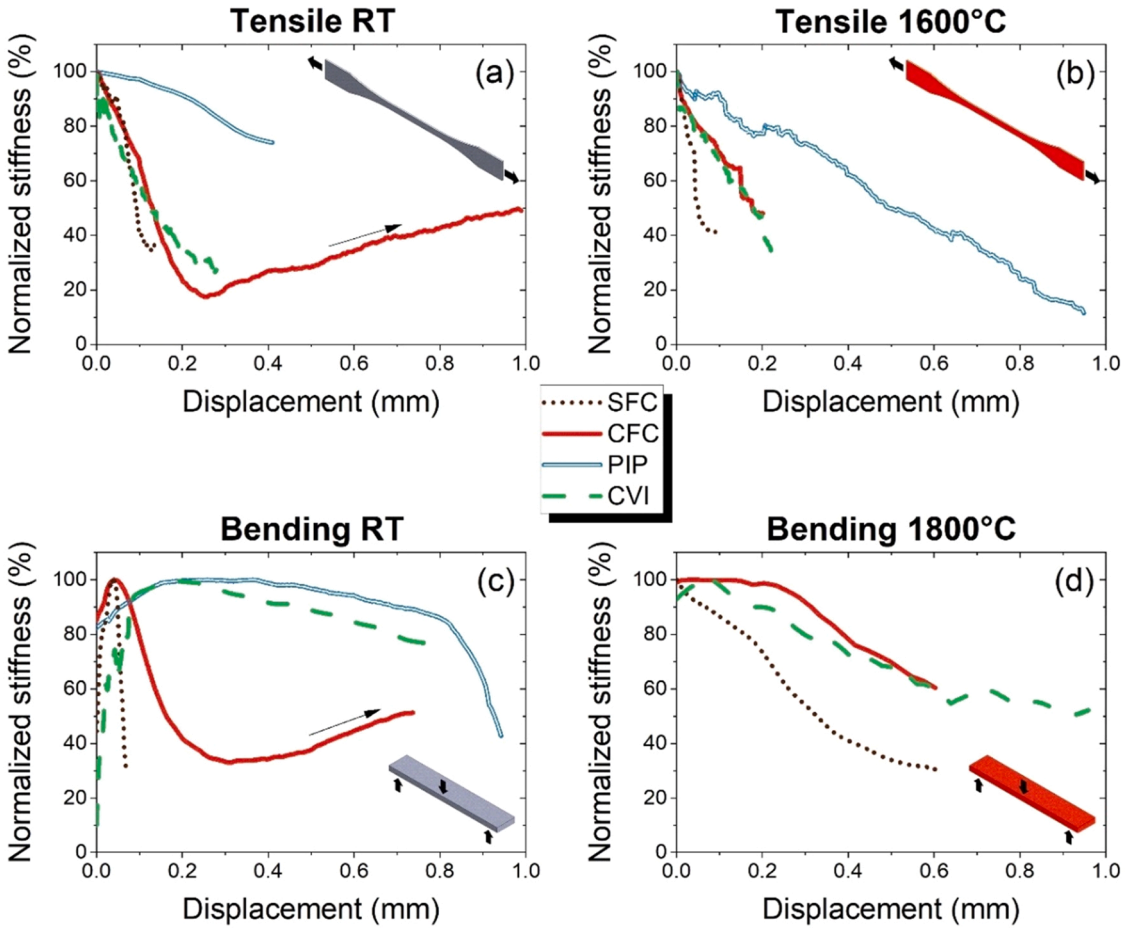

Fig. 13. Normalized stiffness (ratio of stiffness to its maximum value) versus displacement up to failure (the point of maximum force) of tensile tests at (a) RT and (b) 1600 °C, and bending tests at (c) RT and (d) 1800 °C.

part), and the following stretching of the relaxed fibres (increasing part highlighted by the arrow in Fig. 13 a and c), respectively [37]. The lack of this behaviour at high temperature, both for tensile and bending, is further evidence that the RTS are produced during the cooling step of the sintering process owing to the CTE mismatch between fibre and matrix. It is worth noting that SFC material, owing to its matrix-dominated behaviour, does not show the stiffness recovery and the failure occurred at similar displacement values of that corresponding to the matrix-cracking of CFC material (see the matching between the peak of CFC and SCF in Fig. 13 c). A similar observation was done with unidirectional 0/0° CFC tested along fibre axis (fibre dominated behaviour) and transversally to the fibre axis (matrix-dominated behaviour) [37]. In a recent work, in order to limit the matrix dominated-behaviour of SFC composites and enhance the fibre reinforcement, the volumetric fibre amount was increased up to 50% [78]. This increase led to higher displacements and a load–displacement curve similar to the first stage of CFC (Fig. 9b). Currently, the research efforts are aiming to increase the fibre length in order to extend the load-displacement curve of SFC to the second and third stage. As for CFC, the release of the fibre compressive strain led to an expansion of 1508 ± 132 μm/m during tensile tests and 1727 ± 350 μm/m during bending tests. As explained in Ref. [37], this residual strain can be estimated as the difference between the strains at which the stiffness between the strains relative to the minimum and maximum stiffness values in the first derivative of the load-displacement curves. The residual compressive stress of the fibre, calculated with the Hooke's law, is:

$$\sigma_{RTS,fibre} = \varepsilon_{RTS,fibre} E_{fibre} = -0.001508 \bullet 780GPa = -1176MPa \quad (4)$$

$$\sigma_{RTS,fibre} = \varepsilon_{RTS,fibre} E_{fibre} = -0.001727 \bullet 780GPa = -1347MPa \quad (5)$$

according to tensile and bending data: Eq.4 and Eq.5, respectively. The calculated residual stress is lower than the critical value of the fibre (Table 1) and more than double with respect to that calculated for unidirectional 0/0° CFC composite [37]. This result is expected since the fibres amount is equally split in the 0 and 90° orientation. In this case, the estimation of the tensile residual stress within the matrix is more complicated that in case of unidirectional 0/0 ° CFC composite, where the following RTS balance was imposed [37]:

$$\sigma_{RTS,fibre} V_{fibre} + \sigma_{RTS,matrix} V_{matrix} = 0 \quad (6)$$

To consider the role of transverse fibre, V_{fibre} and V_{matrix} of Eq.6 can be taken equal to 0.54/2 and 0.4 + 0.54/2, respectively, where 0.54 is the volumetric fraction of the fibre and 0.4 is the volumetric fraction of the matrix (Table 1). The residual tensile stress of the matrix, averaged on the results of Eq.4 and Eq.5 with the above volume fractions, is 540 ± 220 MPa. This residual tensile stress is lower than the theoretical strength of the matrix (637 ± 80 MPa [79]) and close to that calculated for unidirectional 0/0° CFC composite (589 ± 108 MPa) [37]. However, it is a rougher estimation with respect to that calculated for unidirectional 0/0° CFC composite. This residual tensile stress of the matrix should be intended as an average value since the stress distribution in the 0/90° architecture should be less homogeneous and with stress peaks higher than the 0/0° architecture. This hypothesis is partially supported by the lower off-axis strength of 0/90° CFC composite with respect to that of 0/0° one: 23 ± 9 MPa [35] vs 61 ± 13 MPa [37].

Finally, it is worth noting that the stiffness recovery of 0/90° CFC composite is halved with respect to that showed by 0/0 ° one: 49 ± 7% vs 97 ± 11% [37]. On one hand, tis finding seems to be in agreement with the different architecture, on the other hand the understanding of such high stiffness recovery is still an open issue of these newly developed materials.

4. Conclusions

For the first time, the performance of different types of UHTCMCs are compared based on their stiffness, tensile and flexural strength, and strain capacity at room and high temperature (up to 1800 °C). All the composites yielded good results of tensile tests in terms of the collected data and also in terms of failure mode and location. The sintered short fibre-reinforced composites showed a brittle behaviour and an increase of strength with increasing temperature. The sintered continuous fibre-reinforced composites, which were characterized by 50 vol% of fibre and a dense UHTC matrix, showed a higher damage tolerance and considerable increase of strength with increasing temperature. The highest strength was obtained with continuous fibre-reinforced material produced by filament winding and PIP consolidation technique. With increasing the complexity of the fibre perform, the obtained data became more scattered making difficult a sound comparison. Nevertheless, CVI showed comparable mean value of flexural strength with the other investigated composites. All the ZrB_2-based CMCs demonstrated good structural properties even at 1600–1800 °C and a correlation between mechanical properties and microstructure features well predicted by the conventional models of CMCs. The novel feature in the field of CMCs is the high plasticity reserve of the sintered continuous pitch-derived carbon fibre-reinforced composites. This plasticity reserve is given by residual compressive thermal strains within the fibre of about 1260 μm/m in case of 0/90° architecture.

CRediT authorship contribution statement

Pietro Galizia: Conceptualization, Methodology, Investigation, Formal analysis, Data curation, Visualization, Writing – original draft, Writing – review & editing. **Diletta Sciti:** Conceptualization, Writing – review & editing, Supervision, Project administration, Funding acquisition. **Jon Binner:** Supervision, Validation, Writing - review & editing. **Vinothini Venkatachalam:** Resources, Writing - review & editing. **Miguel.A. Lagos:** Resources. **Francesca Servadei:** Investigation, Writing - review & editing. **Antonio Vinci:** Investigation, Writing - review & editing. **Luca Zoli:** Resources, Writing - review & editing. **Thomas Reimer:** Methodology, Investigation, Validation, Writing – review & editing.

Declaration of Competing Interest

The authors declare that they have no known competing financial interests or personal relationships that could have appeared to influence the work reported in this paper.

Acknowledgements

This work has received funding from the European Union's Horizon 2020 "Research and innovation programme" under grant agreement No 685594 (C3HARME). The authors greatly acknowledge Airbus Defence and Space GmbH for the collaboration and supplying materials.

References

[1] Web Page of C3HARME, (n.d.). ⟨https://c3harme.eu/⟩.
[2] Y. Zhao, Y. Chen, C. He, S. Ai, D. Fang, A damage-induced short-circuit diffusion model applied to the oxidation calculation of ceramic matrix composites (CMCs), Compos. Part A Appl. Sci. Manuf. 127 (2019), 105621, https://doi.org/10.1016/J.COMPOSITESA.2019.105621.
[3] D. Yin, Y. Deng, Y. Ma, X. Fan, Effect of SiC content on the mechanical behaviour of a three-dimensional needled C/SiC composite, Ceram. Int (2021), https://doi.org/10.1016/j.ceramint.2021.05.237.
[4] X. Luan, G. Liu, M. Tian, Z. Chen, L. Cheng, Damage behavior of atomic oxygen on a hafnium carbide-modified C/SiC composite, Compos. Part B Eng. 219 (2021), 108888, https://doi.org/10.1016/j.compositesb.2021.108888.
[5] J.W. Kemp, A.A. Diaz, E.C. Malek, B.P. Croom, Z.D. Apostolov, S.R. Kalidindi, B. G. Compton, L.M. Rueschhoff, Direct Ink Writing of ZrB2-SiC Chopped Fiber Ceramic Composites, Addit. Manuf. 44 (2021), 102049, https://doi.org/10.1016/j.addma.2021.102049.
[6] L. Chen, X. Yang, Z. Su, C. Fang, G. Zeng, Q. Huang, Fabrication and performance of micro-diamond modified C/SiC composites via precursor impregnation and pyrolysis process, Ceram. Int. 44 (2018) 9601–9608, https://doi.org/10.1016/j.ceramint.2018.02.185.
[7] C. Hu, S. Pang, S. Tang, S. Wang, H. Huang, H.M. Cheng, Ablation and mechanical behavior of a sandwich-structured composite with an inner layer of Cf/SiC between two outer layers of Cf/SiC-ZrB2-ZrC, Corros. Sci. 80 (2014) 154–163, https://doi.org/10.1016/j.corsci.2013.11.019.
[8] S. Tang, J. Deng, S. Wang, W. Liu, Comparison of thermal and ablation behaviors of C/SiC composites and C/ZrB2-SiC composites, Corros. Sci. 51 (2009) 54–61, https://doi.org/10.1016/j.corsci.2008.09.037.
[9] D. Zhang, P. Hu, S. Dong, X. Liu, C. Wang, Z. Zhang, X. Zhang, Oxidation behavior and ablation mechanism of Cf/ZrB2-SiC composite fabricated by vibration-assisted slurry impregnation combined with low-temperature hot pressing, Corros. Sci. 161 (2019), 108181, https://doi.org/10.1016/j.corsci.2019.108181.
[10] H. Ouyang, Y. Zhang, C. Li, G. Li, J. Huang, H. Li, Effects of ZrC/SiC ratios on mechanical and ablation behavior of C/C–ZrC–SiC composites prepared by carbothermal reaction of hydrothermal co-deposited oxides, Corros. Sci. 163 (2019), 108239, https://doi.org/10.1016/j.corsci.2019.108239.
[11] B.W. Chen, D.W. Ni, C.J. Liao, Y.L. Jiang, J. Lu, S.M. Dong, Long-term ablation behavior and mechanisms of 2D-Cf/ZrB2-SiC composites at temperatures up to 2400 °C, Corros. Sci. 177 (2020), 108967, https://doi.org/10.1016/j.corsci.2020.108967.
[12] D. Huang, M. Zhang, Q. Huang, L. Wang, L. Xue, X. Tang, K. He, Ablation mechanism of C/C-ZrB2-ZrC-SiC composite fabricated by polymer infiltration and pyrolysis with preform of Cf/ZrB2, Corros. Sci. 98 (2015) 551–559, https://doi.org/10.1016/j.corsci.2015.05.064.
[13] L. Zhuang, Q.G. Fu, T.Y. Liu, Ablation resistance of wedge-shaped C/C-ZrB2-ZrC-SiC composites exposed to an oxyacetylene torch, Corros. Sci. 112 (2016) 462–470, https://doi.org/10.1016/j.corsci.2016.08.010.
[14] L.M. Rueschhoff, C.M. Carney, Z.D. Apostolov, M.K. Cinibulk, Processing of fiber-reinforced ultra-high temperature ceramic composites: A review, Int. J. Ceram. Eng. Sci. 2 (2020) 22–37, https://doi.org/10.1002/ces2.10033.
[15] H. Hald, Operational limits for reusable space transportation systems due to physical boundaries of C/SiC materials, Aerosp. Sci. Technol. 7 (2003) 551–559, https://doi.org/10.1016/S1270-9638(03)00054-3.
[16] X. Wang, K. Wei, Y. Tao, X. Yang, H. Zhou, R. He, D. Fang, Thermal protection system integrating graded insulation materials and multilayer ceramic matrix composite cellular sandwich panels, Compos. Struct. 209 (2019) 523–534, https://doi.org/10.1016/J.COMPSTRUCT.2018.11.004.
[17] W. Xie, Z. Peng, S. Meng, C. Xu, F. Yi, H. Jin, S. Du, Thermal stress analysis of the FGLCS in hypersonic vehicles: Their application to fuel injection struts in scramjets, Compos. Part A Appl. Sci. Manuf. 99 (2017) 157–165, https://doi.org/10.1016/J.COMPOSITESA.2017.03.034.
[18] Z. Peng, W. Sun, X. Xiong, Z. Zhan, J. Li, Comparative insights into C/C–ZrC–SiC composites with different substrate carbon on microstructures, mechanical properties, and ablation behaviors, J. Mater. Res. Technol. 14 (2021) 662–676, https://doi.org/10.1016/J.JMRT.2021.06.089.
[19] X. Xu, X. Luan, J. Zhang, X. Cao, D. Zhao, L. Cheng, R. Riedel, Significant improvement of ultra-high temperature oxidation resistance of C/SiC composites upon matrix modification by SiHfBCN ceramics, Compos. Part B Eng. 253 (2023), 110553, https://doi.org/10.1016/J.COMPOSITESB.2023.110553.
[20] B.W. Chen, D.W. Ni, J. Lu, F.Y. Cai, X.G. Zou, H.J. Zhou, S.M. Dong, Multi-cycle and long-term ablation behavior of Cf/ZrB2-SiC composites at 2500 °C, Corros. Sci. 184 (2021), 109385, https://doi.org/10.1016/j.corsci.2021.109385.
[21] Y. Arai, R. Inoue, K. Goto, Y. Kogo, Carbon fiber reinforced ultra-high temperature ceramic matrix composites: A review, Ceram. Int. 45 (2019) 14481–14489, https://doi.org/10.1016/j.ceramint.2019.05.065.
[22] J. Binner, M. Porter, B. Baker, J. Zou, V. Venkatachalam, V.R. Diaz, A. D'Angio, P. Ramanujam, T. Zhang, T.S.R.C. Murthy, Selection, processing, properties and applications of ultra-high temperature ceramic matrix composites, UHTCMCs – a review, Int. Mater. Rev. (2019) 1–56, https://doi.org/10.1080/09506608.2019.1652006.
[23] D. Zhang, J. Feng, P. Hu, L. Xun, M. Liu, S. Dong, X. Zhang, Enhanced mechanical properties and thermal shock resistance of Cf/ZrB2-SiC composite via an efficient slurry injection combined with vibration-assisted vacuum infiltration, J. Eur. Ceram. Soc. (2020), https://doi.org/10.1016/j.jeurceramsoc.2020.07.003.
[24] P. Hu, Y. Cheng, D. Zhang, L. Xun, M. Liu, C. Zhang, X. Zhang, S. Du, From ferroconcrete to Cf/UHTC-SiC: A totally novel densification method and mechanism at 1300 °C without pressure, Compos. Part B Eng. 174 (2019), 107023, https://doi.org/10.1016/j.compositesb.2019.107023.
[25] Y. Liu, Y. Zu, H. Tian, J. Dai, J. Sha, Microstructure and mechanical properties of continuous carbon fiber-reinforced ZrB2-based composites via combined electrophoretic deposition and sintering, J. Eur. Ceram. Soc. (2020), https://doi.org/10.1016/j.jeurceramsoc.2020.10.044.

[26] H. Istgaldi, B. Nayebi, Z. Ahmadi, P. Shahi, M. Shahedi Asl, Characterization of ZrB2–TiC composites reinforced with short carbon fibers, Ceram. Int. 46 (2020) 23155–23164, https://doi.org/10.1016/j.ceramint.2020.06.095.
[27] P. Galizia, A. Vinci, L. Zoli, F. Monteverde, J. Binner, V. Venkatachalam, M. A. Lagos, T. Reimer, N. Jain, D. Sciti, Retained strength of UHTCMCs after oxidation at 2278 K, Compos. Part A Appl. Sci. Manuf. 149 (2021), 106523, https://doi.org/10.1016/j.compositesa.2021.106523.
[28] P. Galizia, L. Zoli, D. Sciti, Impact of residual stress on thermal damage accumulation, and Young's modulus of fiber-reinforced ultra-high temperature ceramics, Mater. Des. 160 (2018) 803–809, https://doi.org/10.1016/J.MATDES.2018.10.019.
[29] P. Galizia, D. Sciti, F. Saraga, L. Zoli, Off-axis damage tolerance of fiber-reinforced composites for aerospace systems, J. Eur. Ceram. Soc. 40 (2020) 2691–2698, https://doi.org/10.1016/j.jeurceramsoc.2019.12.038.
[30] T. Cheng, Understanding the ultra-high-temperature mechanical behaviors of advanced two-dimensional carbon-carbon composites, Ceram. Int. (2020), https://doi.org/10.1016/j.ceramint.2020.05.237.
[31] L. Li, Modeling Temperature-Dependent Vibration Damping in C/SiC Fiber-Reinforced Ceramic-Matrix Composites, Mater. (Basel) 13 (2020) 1633, https://doi.org/10.3390/ma13071633.
[32] K. Vaferi, M. Vajdi, S. Nekahi, S. Nekahi, F. Sadegh Moghanlou, M. Shahedi Asl, M. Mohammadi, Thermo-mechanical simulation of ultrahigh temperature ceramic composites as alternative materials for gas turbine stator blades, Ceram. Int. 47 (2021) 567–580, https://doi.org/10.1016/j.ceramint.2020.08.164.
[33] P. Galizia, D. Sciti, N. Jain, Insight into microstructure and flexural strength of ultra-high temperature ceramics enriched SICARBON™ composite, Mater. Des. (2021), 109888, https://doi.org/10.1016/j.matdes.2021.109888.
[34] B. Baker, V. Rubio, P. Ramanujam, J. Binner, A. Hussain, T. Ackerman, P. Brown, I. Dautremont, Development of a slurry injection technique for continuous fibre ultra-high temperature ceramic matrix composites, J. Eur. Ceram. Soc. 39 (2019) 3927–3937, https://doi.org/10.1016/j.jeurceramsoc.2019.05.070.
[35] D. Sciti, L. Zoli, T. Reimer, A. Vinci, P. Galizia, A systematic approach for horizontal and vertical scale up of sintered Ultra-High Temperature Ceramic Matrix Composites for aerospace – Advances and perspectives, Compos. Part B Eng. 234 (2022), 109709, https://doi.org/10.1016/J.COMPOSITESB.2022.109709.
[36] B. Harris, E. Institute of Materials (London, Engineering composite materials, IOM,, London, 1999. ⟨https://books.google.it/books/about/Engineering_Composite_Materials.html?id=9MVRAAAAMAAJ&redir_esc=y⟩. accessed November 24, 2017.
[37] P. Galizia, D. Sciti, Disclosing residual thermal stresses in UHT fibre-reinforced ceramic composites and their effect on mechanical behaviour and damage evolution, Compos. Part B Eng. 248 (2023), 110369, https://doi.org/10.1016/J.COMPOSITESB.2022.110369.
[38] P. Galizia, S. Failla, L. Zoli, D. Sciti, Tough salami-inspired Cf/ZrB2 UHTCMCs produced by electrophoretic deposition, J. Eur. Ceram. Soc. 38 (2018) 403–409, https://doi.org/10.1016/j.jeurceramsoc.2017.09.047.
[39] P. Morgan, Carbon fibers and their composites, Taylor & Francis,, 2005.
[40] W.G. Fahrenholtz, G.E. Hilmas, I.G. Talmy, J.A. Zaykoski, Refractory Diborides of Zirconium and Hafnium, J. Am. Ceram. Soc. 90 (2007) 1347–1364, https://doi.org/10.1111/j.1551-2916.2007.01583.x.
[41] B. Raju Golla, A. Mukhopadhyay, B. Basu, S. Kumar Thimmappa, Review on Ultra High Temperature Boride Ceramics, Prog. Mater. Sci. (2020), 100651, https://doi.org/10.1016/j.pmatsci.2020.100651.
[42] W.-C. Tu, F.F. Lange, A.G. Evans, Concept for a Damage-Tolerant Ceramic Composite with "Strong" Interfaces, J. Am. Ceram. Soc. 79 (1996) 417–424, https://doi.org/10.1111/j.1151-2916.1996.tb08138.x.
[43] E.A.V. Carelli, H. Fujita, J.Y. Yang, F.W. Zok, Effects of Thermal Aging on the Mechanical Properties of a Porous-Matrix Ceramic Composite, J. Am. Ceram. Soc. 85 (2004) 595–602, https://doi.org/10.1111/j.1151-2916.2002.tb00138.x.
[44] J.P. Singh, N.P. Bansal, T. Goto, J. Lamon, S.R. Choi, M.M. Mahmoud, G. Link, Processing and Properties of Advanced Ceramics and Composites IV, John Wiley & Sons, Inc,, Hoboken, NJ, USA, 2012, https://doi.org/10.1002/9781118491867.
[45] U. Santhosh, J. Ahmad, T. Easler, Y. Gowayed, A Polymer Infiltration and Pyrolysis (PIP) Process Model for Ceramic Matrix Composites (CMCs), J. Am. Ceram. Soc. (2021), https://doi.org/10.1111/jace.17966.
[46] Z. Tang, M. Yi, Q. Xiang, Y. Du, K. Peng, Mechanical and ablation properties of a C/C-HfB2-SiC composite prepared by high-solid-loading slurry impregnation combined with precursor infiltration and pyrolysis, J. Eur. Ceram. Soc. (2021), https://doi.org/10.1016/j.jeurceramsoc.2021.06.055.
[47] X. Zou, D. Ni, B. Chen, L. Ye, Y. Sun, J. Lu, F. Cai, L. Gao, T. Zhao, S. Dong, Fabrication and properties of C_f /Ta_4HfC_5 -SiC composite via precursor infiltration and pyrolysis (jace), J. Am. Ceram. Soc. (2021) 18007, https://doi.org/10.1111/JACE.18007.
[48] D. Zhang, H. Yu, A. Wang, P. Hu, L. Ren, D. Sun, Ablation behavior and mechanisms of 3D Cf/ZrB2-SiC composite applied in long-term temperature up to 2400 °C, Corros. Sci. 190 (2021), 109706, https://doi.org/10.1016/J.CORSCI.2021.109706.
[49] F. Servadei, L. Zoli, P. Galizia, A. Piancastelli, D. Sciti, Processing and characterization of ultra-high temperature ceramic matrix composites via water based slurry impregnation and polymer infiltration and pyrolysis, Ceram. Int (2022), https://doi.org/10.1016/J.CERAMINT.2022.09.100.
[50] J.J. Sha, J. Li, S.H. Wang, Z.F. Zhang, Y.F. Zu, S. Flauder, W. Krenkel, Improved microstructure and fracture properties of short carbon fiber-toughened ZrB2-based UHTC composites via colloidal process, Int. J. Refract. Met. Hard Mater. 60 (2016) 68–74, https://doi.org/10.1016/j.ijrmhm.2016.07.010.
[51] S. Hofmann, Effect of interlaminar defects on the mechanical behaviour of carbon fibre reinforced silicon carbide, Universität Stuttgart, 2014. ⟨https://elib.dlr.de/87469/⟩ (accessed February 5, 2020).
[52] C.G. Papakonstantinou, P. Balaguru, R.E. Lyon, Comparative study of high temperature composites, Compos. Part BEngineering 32 (2001) 637–649, https://doi.org/10.1016/S1359-8368(01)00042-7.
[53] P.S. Steif, A. Trojnacki, Bend Strength versus Tensile Strength of Fiber-Reinforced Ceramics, J. Am. Ceram. Soc. 77 (1994) 221–229, https://doi.org/10.1111/J.1151-2916.1994.TB06981.X.
[54] F. Hild, J.M. Domergue, F.A. Leckie, A.G. Evans, Tensile and flexural ultimate strength of fiber-reinforced ceramic-matrix composites, Int. J. Solids Struct. 31 (1994) 1035–1045, https://doi.org/10.1016/0020-7683(94)90010-8.
[55] D. Aveston, A. Kelly, Theory of multiple fracture of fibrous composites, J. Mater. Sci. 8 (1973) 352–362, https://doi.org/10.1007/BF00550155.
[56] L. Zoli, A. Vinci, P. Galizia, C. Melandri, D. Sciti, On the thermal shock resistance and mechanical properties of novel unidirectional UHTCMCs for extreme environments, Sci. Rep. 8 (2018) 9148, https://doi.org/10.1038/s41598-018-27328-x.
[57] S. Onodera, J. Tsuyuki, T. Okabe, Micromechanical modeling for the in-plane mechanical behavior of orthogonal three-dimensional woven ceramic matrix composites with transverse and matrix cracking:, Https://Doi.Org/10.1177/10567895211026017. (2021) 105678952110260. https://doi.org/10.1177/10567895211026017.
[58] L. Li, A micromechanical loading/unloading constitutive model of fiber-reinforced ceramic-matrix composites considering matrix crack closure (ffe), Fatigue Fract. Eng. Mater. Struct. (2021) 13509, https://doi.org/10.1111/ffe.13509.
[59] S. Hönig, D. Koch, S. Weber, S. Etzold, T. Tonnesen, R. Telle, N. Traon, Evaluation of dynamic modulus measurement for C/C-SiC composites at different temperatures, Int. J. Appl. Ceram. Technol. 16 (2019) 1723–1733, https://doi.org/10.1111/ijac.13293.
[60] W. Krenkel, Carbon Fibre Reinforced Silicon Carbide Composites (C/SiC, C/C-SiC). Handb. Ceram. Compos, Springer US,, 2006, pp. 117–148, https://doi.org/10.1007/0-387-23986-3_6.
[61] S. Kumar, A. Painuly, A. Kamal, S. Kuttappan, R.R. Kumar, S.P. Prabhakaran, R. Devasia, Development of C/SiC Fasteners for High-Temperature Applications, Mater. Perform. Charact. 10 (2021), 20200161, https://doi.org/10.1520/MPC20200161.
[62] D. Sciti, P. Galizia, T. Reimer, A. Schoberth, C.F. Gutiérrez-Gonzalez, L. Silvestroni, A. Vinci, L. Zoli, Properties of large scale ultra-high temperature ceramic matrix composites made by filament winding and spark plasma sintering, Compos. Part B Eng. (2021), https://doi.org/10.1016/j.compositesb.2021.108839.
[63] A. Vinci, L. Zoli, P. Galizia, D. Sciti, Influence of Y2O3 addition on the mechanical and oxidation behaviour of carbon fibre reinforced ZrB2/SiC composites, J. Eur. Ceram. Soc. (2020), https://doi.org/10.1016/j.jeurceramsoc.2020.06.043.
[64] D. Sciti, L. Zoli, A. Vinci, L. Silvestroni, S. Mungiguerra, P. Galizia, Effect of PAN-based and pitch-based carbon fibres on microstructure and properties of continuous Cf/ZrB2-SiC UHTCMCs, J. Eur. Ceram. Soc. 41 (2020) 3045–3050, https://doi.org/10.1016/j.jeurceramsoc.2020.05.032.
[65] C. Sauder, J. Lamon, R. Pailler, The tensile behavior of carbon fibers at high temperatures up to 2400 °C, Carbon N. Y 42 (2004) 715–725, https://doi.org/10.1016/j.carbon.2003.11.020.
[66] T. Cheng, X. Wang, R. Zhang, Y. Pei, S. Ai, R. He, D. Fang, Y. Yang, Tensile properties of two-dimensional carbon fiber reinforced silicon carbide composites at temperatures up to 2300 °C, J. Eur. Ceram. Soc. 40 (2020) 630–635, https://doi.org/10.1016/j.jeurceramsoc.2019.10.030.
[67] Y. Zhang, L. Zhang, L. Cheng, Y. Xu, Tensile behavior and microstructural evolution of a carbon/silicon carbide composite in simulated re-entry environments, Mater. Sci. Eng. A 473 (2008) 111–118, https://doi.org/10.1016/j.msea.2007.05.015.
[68] J. Koyanagi, H. Hatta, M. Kotani, H. Kawada, A Comprehensive Model for Determining Tensile Strengths of Various Unidirectional Composites, J. Compos. Mater. 43 (2009) 1901–1914, https://doi.org/10.1177/0021998309341847.
[69] Z. Wang, G. Fang, B. Wang, P. Hu, F. Yi, S. Meng, Study on toughening mechanisms of pyrolytic carbon interface layer in Cf/ZrB2-SiC composites using in-situ tensile experimental and numerical methods, J. Eur. Ceram. Soc. (2021), https://doi.org/10.1016/j.jeurceramsoc.2021.04.028.
[70] F. Servadei, L. Zoli, P. Galizia, C. Melandri, D. Sciti, Preparation of UHTCMCs by hybrid processes coupling Polymer Infiltration and Pyrolysis with Hot Pressing and vice versa, J. Eur. Ceram. Soc. 42 (2022) 2118–2126, https://doi.org/10.1016/J.JEURCERAMSOC.2021.12.039.
[71] V. Rubio, J. Binner, S. Cousinet, G. Le Page, T. Ackerman, A. Hussain, P. Brown, I. Dautremont, Materials characterisation and mechanical properties of Cf-UHTC powder composites, J. Eur. Ceram. Soc. 39 (2019) 813–824, https://doi.org/10.1016/J.JEURCERAMSOC.2018.12.043.
[72] J. Cohen. Statistical Power Analysis for the Behavioral Sciences, 2nd ed..,, Lawrence Erlbaum Associates,, 1988.
[73] C. Pradere, C. Sauder, Transverse and longitudinal coefficient of thermal expansion of carbon fibers at high temperatures (300–2500 K), Carbon N. Y 46 (2008) 1874–1884, https://doi.org/10.1016/j.carbon.2008.07.035.
[74] R.W. Rice, Evaluation and extension of physical property-porosity models based on minimum solid area, J. Mater. Sci. 31 (1996) 102–118, https://doi.org/10.1007/BF00355133.
[75] M.A. Mattoni, J.Y. Yang, C.G. Levi, F.W. Zok, Effects of Matrix Porosity on the Mechanical Properties of a Porous-Matrix, All-Oxide Ceramic Composite, J. Am. Ceram. Soc. 84 (2001) 2594–2602, https://doi.org/10.1111/J.1151-2916.2001.TB01059.X.

[76] J. Lemaitre, J. Dufailly, Damage measurements, Eng. Fract. Mech. 28 (1987) 643–661, https://doi.org/10.1016/0013-7944(87)90059-2.
[77] A. Shojaei, G. Li, J. Fish, P.J. Tan, Multi-scale constitutive modeling of Ceramic Matrix Composites by Continuum Damage Mechanics, Int. J. Solids Struct. 51 (2014) 4068–4081, https://doi.org/10.1016/J.IJSOLSTR.2014.07.026.
[78] M. Mor, A. Vinci, S. Failla, P. Galizia, L. Zoli, D. Sciti, A novel approach for manufacturing of layered, ultra-refractory composites using pliable, short fibre-reinforced ceramic sheets (n.d.), J. Adv. Ceram. (2023) 155–168, https://doi.org/10.26599/JAC.2023.9220674.
[79] F. Monteverde, S. Guicciardi, C. Melandri, D.D. Fabbriche, Densif., Microstruct. Evol. Mech. Prop. Ultra Sci. Part. -Dispersed ZrB2 Matrix Compos. (2010) 261–272, https://doi.org/10.1007/978-90-481-9818-4_17.
[80] P. Gutmann, J. Moosburger-Will, S. Kurt, Y. Xu, S. Horn, Carbonization of polyacrylonitrile-based fibers under defined tensile load: influence on shrinkage behavior, microstructure, and mechanical properties, Polym. Degrad. Stab. 163 (2019) 174–184, https://doi.org/10.1016/j.polymdegradstab.2019.03.007.